

Received December 15, 2020, accepted December 20, 2020, date of publication December 30, 2020, date of current version January 8, 2021.

Digital Object Identifier 10.1109/ACCESS.2020.3048193

# Peak to Average Power Ratio Based Signal Detection for Frequency Shift Multitone SWIPT System

TAKASHI IKEUCHI<sup>1</sup>, (Member, IEEE), AND YOSHIHIRO KAWAHARA<sup>2</sup>, (Member, IEEE)

<sup>1</sup>Department of Information Science and Technology, The University of Tokyo, Tokyo 113-8654, Japan

<sup>2</sup>Department of Electrical Engineering, The University of Tokyo, Tokyo 113-8654, Japan

Corresponding author: Takashi Ikeuchi (ikeuchi@akg.t.u-tokyo.ac.jp)

This work was supported in part by the JST ERATO under Grant JPMJER1501, and in part by the VLSI Design and Education Center (VDEC), The University of Tokyo, with the collaboration with Keysight Technologies.

**ABSTRACT** In this paper, we investigate a multitone simultaneous wireless information and power transfer (SWIPT) based modulation scheme for battery-less Internet of Things (IoT) nodes that works in the ultra high frequency (UHF) region. The conventional SWIPT system is assumed to have power-consuming communication modules. Having such modules on to the IoT nodes whose power is harvested from radio frequency (RF) power sources is too unrealistic. In addition, waveform design from the aspect of power harvesting through SWIPT still has room for consideration. Recent studies have explored multitone based SWIPT to increase the power conversion efficiency (PCE). In these schemes, information is modulated by changing each tone's nature or varying the number of tones. Among these methods, we focused on modulation schemes known as frequency-shift multitone based SWIPT, which shifts frequencies among the tones for information encoding. Unlike previously proposed methods where demodulation requires some power-consuming fast Fourier transfers (FFTs), especially under small communication bandwidths, we applied a signal detection method by measuring output peak to average power ratios (PAPRs) for frequency-shift multitone based SWIPT to reduce power consumption. Based on our analysis, different tone configurations in the frequency domain would yield varieties of nonlinear outputs during the rectification process. In addition, these specific nonlinear output patterns depend on the tone configurations. With this feature, it is possible to demodulate in the time domain at the receiver side using PAPR based measurements, which could eliminate FFT operation. This paper describes how measuring PAPRs enables the detection of signals in theory and validates this through simulations and experiments. We also estimate the communication rates. Based on our results, we achieved 0.46 bits/s/Hz when the number of tones was 6 and estimated that there were  $(N - 1)(N - 2)/2 + 1$  different PAPRs from a given multitone waveform whose number of tones was  $N$ .

**INDEX TERMS** Energy harvesting, frequency shift keying, multisine based waveforms, peak to average ratio, simultaneous wireless information and power transfer.

## I. INTRODUCTION

The Internet of Things (IoT) has gained much attention as billions of devices can be connected through networks capturing information and influencing our decisions in our daily lives [1]. However, as numerous devices are installed everywhere, battery management is becoming cumbersome, as most of them require batteries or wired power sources.

The associate editor coordinating the review of this manuscript and approving it for publication was Chien-Ming Chen<sup>1</sup>.

Eliminating batteries would ease the recharging processes; devices would sustainably exist ubiquitously and seamlessly around us [2]. These devices need external power sources for the substitution of batteries, and among the emerging energy harvesting methods, wireless power transfer (WPT) method is attractive. This is because devices can obtain RF transmitted power based on their needs instead of harvesting occasionally from solar power, vibration, or other harvesting technologies. Among the wireless power transmission methods, we aim to utilize the radio frequency (RF) power harvesting

method instead of coupling based methods so that the devices can be operated without being in close proximity to the transmitter [3].

It has been revealed that using the same waveforms, not only power but also information can be delivered, known as simultaneous wireless and information power transfer (SWIPT). In such context, the information is superimposed on wireless power transferred waveforms [4]–[8]. In addition, it is possible to share the antennas for information and power reception, which is attractive in terms of reducing additional costs for embedding extra antennas and meeting the requirements for a small form factor of IoT devices.

However, realizing the SWIPT system with high speed and high power efficiency is challenging for battery-less IoT nodes since its low power operation restricts the conventional communication method, which uses power-hungry RF front end (power amplifiers, local oscillators, etc) [3], [9]. Recently, a method for optimizing power allocation for communication and power harvesting for a nonlinear circuit has been proposed [10]. However, designing SWIPT waveforms based on conventional communication modules is still a challenging task. In specific, it is necessary to design transmit waveforms such that IoT nodes can handle wireless information without using active devices that would reduce the power efficiency.

Recently, a multitone RF harvesting method has been proposed in order to produce higher power conversion efficiency (PCE) with the same transmit power compared with continuous wave (CW) power harvesting waveforms [5], [11], [12]. This waveform consists of summations of multiple sine waves and produces high peak-to-average power ratios (PAPRs). This nature gives a higher PCE at the receiver node due to the nonlinearity effects of diodes in the rectifiers. Therefore, using these waveforms has more advantages than continuous wave (CW) [13]–[15].

In addition, this multitone waveform can also be used for conveying information without the need for power-hungry elements; this is called multitone SWIPT. Since nonlinear elements output intermodulation products of the input waveform, it is possible to generate varieties of outputs using multitone waveforms. Therefore, differently designed input waveforms can be distinguishable by measuring the rectified outputs.

Multitone SWIPT can be realized by arranging the amplitudes, frequencies, phases of each tone or by varying the number of tones [11], [16]–[19]. Among these methods, modulation based on the number of tones is one of the attractive approaches in that it uses PAPR fluctuations by varying the number of tones in the transmitted waveform [20], [21]. These authors revealed the tradeoff between the communication rate and the direct current (DC) supply capability. While an increased number of tones results in larger rectified voltage, the communication rate becomes poor. This is due to the fact that increasing the number of tones in a fixed bandwidth results in shortening the frequency spacing. Since the communication rate severely depends on the frequency

spacing, shortening frequency spacing leads to having poor communication rate. On the other hand, if the number of tones is minimized, the communication rate can be maximized, but the PCE performance does not improve so much. Therefore, it is important to design the waveforms based on the requirements of the SWIPT devices, which is also discussed in [22].

Frequency shift-type SWIPT has been considered as one of the solutions to increase the modulation orders within the same number of tones [22]. In this method, the spacing of the frequency tones is varied in order to perform modulation. They employ the intermodulation products of the harmonic signal generated by the diodes in the rectifiers to retrieve information. Since different frequency tone configurations generate different intermodulation products, the receiver could solve the inverse problem by evaluating the spectrum of the waveform in the frequency domain. This enables the use of higher-order modulation within the same number of tones. However, in most cases, fast Fourier transfer (FFT) is applied to acquire the variations of frequency spacing in this scheme, which is more challenging for battery-less devices to implement in terms of calculation cost. Therefore, achieving high-performance communication while maintaining high PCE with simple receiver hardware is a challenging task. It is true that a passive bandpass filter bank can be used for frequency separation instead of calculating FFTs. However, especially when the communication bandwidth is small, designing a passband passive filter becomes challenging due to the requirement of a high Q factor. For example, at UHF, the passive bandpass filter needs to have a bandwidth of at least 1.5 MHz, which means that tones that reside within 1.5 MHz cannot be differentiated through the filter. Therefore, at UHF, where communication is typically suppressed under 1 MHz, conventional multitone FSK SWIPT needs to rely on the FFT calculation.

In this paper, we applied a PAPR based signal detection method to the frequency shift-type multitone SWIPT scheme. Based on our analysis, different tone configurations in the frequency domain yield varieties of nonlinear outputs from a rectifier. In addition, specific nonlinear output patterns depend on the tone configurations. Due to this feature, it is possible to demodulate a signal at the receiver side in the time domain instead of in the frequency domain by introducing PAPR based measurements. This makes it possible to demodulate frequency shift-type SWIPT with a simple circuit structure. Our contributions are the following;

- We showed the principles of how frequency shift tones change the PAPRs at the receiver side and demonstrate the validity of the scheme through simulation and experiments.
- We estimated and verified how many PAPRs could be produced with the same number of tones and investigated the communication rate with the optimal tone configurations.
- We verified that our introduced receiver circuit can differentiate all the possible PAPRs generated by the same

number of tones through circuit simulation as well as experiments.

This paper is structured as follows. In Section II, we show the relationship between the configuration of tones and the PAPR values of the outputs at the receiver side. In Section III, we categorize the tone configurations based on the PAPRs, and estimate how many different PAPRs could be generated within the same number of tones. In addition, we estimate the maximal communication rate. Then, in Section IV, we introduce the receiver circuit that can realize this idea and show the feasibility of the PAPR based method. We compared the with the most related method in Section. V. Finally, we conclude this paper in Section VI.

## II. PAPR BASED SIGNAL DETECTION PRINCIPLE

### A. SIGNAL DESCRIPTION

Multisine based waveforms  $x_T(t)$  at a transmitter are modeled as follows;

$$x_T(t) = \text{Re} \left\{ \sum_{i=1}^N \sqrt{\frac{P_T R_{TxAnt}}{N}} \exp(j(\omega_i t + \phi_i)) \right\}, \quad (1)$$

where  $N$ ,  $P_T$ ,  $R_{TxAnt}$ ,  $\omega_i$ , and  $\phi_i$  represent the number of tones, the transmit power, the impedance of the transmitter antenna, the angular frequency of the  $i$ th tone that is equal to  $2\pi f_i$ , and the phase of the  $i$ th tone, respectively. Here,  $f_i$  is a carrier frequency of the  $i$ th tone. We assume that each fundamental tone has the condition;

$$f_i < f_j, \quad \text{for } i < j \in N. \quad (2)$$

In addition, the bandwidth  $BW$  is fixed, so  $f_N - f_1$  always becomes  $BW$ .

At the receiver side, when the impedance between the antenna and the input impedance seen from the antenna to the rest of the circuit ( $R_{in}$ ) are matched, the received power ( $P_R$ ) that is consumed at the impedance  $R_{in}$  can be derived using Friss's equation [23];

$$P_R = P_T G_T G_R \left( \frac{\lambda}{4\pi d} \right)^2, \quad (3)$$

where  $G_T$ ,  $G_R$ ,  $\lambda$ , and  $d$  are the transmitter gain, the receiver gain, the wavelength of the traversing signal, and the distance between the transmitter and the receiver, respectively. Therefore, the received signal  $y_R(t)$  can be expressed as;

$$y_R(t) = \sqrt{P_T G_T G_R \left( \frac{\lambda}{4\pi d} \right)^2} R_{in}. \quad (4)$$

Here, we assume that the antenna impedance of the receiver and transmitter sides are the same. In addition, we assume that the antenna impedance and the impedance of the following circuit system are the same at the receiver side. In such condition, the excited voltage at the receiver circuit ( $v_{in}(t)$ ) is the same as  $y_R(t)$ . Since  $P_T = E\{x_T^2(t)/R_{in}\}$ , the excited voltage is expressed as  $v_{in}(t) = h x_T(t)$ , where  $h$  is the degradation factor.

### B. HARMONIC SIGNAL GENERATION AND RECTIFICATION

During the process of the rectification, diodes in the receiver circuit generate harmonic signals, and they modulate with each other due to the diodes' nonlinearity [24]. As a result, the signals are downconverted to the baseband (BB) region. The harmonic signals ( $v_{inh}(t)$ ) become the following;

$$\begin{aligned} v_{inh}(t) &= h \{ C_1 x_T(t) + (C_2 x_T(t))^2 + (C_3 x_T(t))^3 + \dots \} \\ &= C'_1 x_T(t) + (C'_2 x_T(t))^2 + (C'_3 x_T(t))^3 + \dots, \end{aligned} \quad (5)$$

where  $C'_1 = h C_1$ ,  $C'_2 = \sqrt[2]{h} C_2$ ,  $C'_3 = \sqrt[3]{h} C_3$ . For example, if a 3-tone signal is transmitted, the transmitted and excited voltage at the receiver side would become following;

$$\begin{aligned} x_T(t) &= \sum_{i=1}^N a \cos(\omega_i t), \quad (6) \\ v_{inh}(t) &= \frac{3}{2} C_2'^2 a^2 \\ &\quad + C_2'^2 a^2 \sum_{i < j} \cos(\omega_i t - \omega_j t) \\ &\quad + \left\{ C_1' a + \frac{15}{4} C_3'^3 a^3 \right\} \sum_{i=1}^3 \cos(\omega_i t) \\ &\quad + \frac{3}{4} C_3'^3 a^3 \left\{ \sum_{i < j} \cos(2\omega_i t - \omega_j t) \right\} \\ &\quad + \frac{3}{2} C_3'^3 a^3 \left\{ \sum_{i \neq j \neq k, i < j} \cos(\omega_i t + \omega_j t - \omega_k t) \right\} \\ &\quad + \text{higher - order terms}, \end{aligned} \quad (7)$$

where  $a = \sqrt{\frac{P_T}{N}}$ , and we assume that up to a 3rd order signal would be generated through the diode, and the input waveform contains 3 tones in this case. Among the higher order terms in Eq. (7), the direct current (DC) term and the second order intermodulation products (IM2) terms dominate the output behaviors [24]. The latter terms in Eq. (7) consist of the frequency differences between the fundamental tones, which indicates that these tones are scattered around the baseband region, and the farthest tones are located as  $f_N - f_1 = BW$ . The waveforms of the output voltage change depending on the arrangement of the tones in the frequency domain.

In addition, the output voltage behaviors are affected by the RC design of the rectifiers. According to the previous papers, the cutoff frequencies of the RC filter in the rectifiers can be determined by  $F_{cutoff} = \frac{1}{2\pi R_L C_L}$  [25]. When the rectified signal contains the tones that have frequencies higher than the  $F_{cutoff}$ , these tones are ceased and the output waveform does not contain the ceased tones in the frequency domain. Therefore, a tradeoff exists between the arrangement of the IM2s and the cutoff frequencies. In order to discuss the tradeoff between the tone arrangement and the output waveform behavior, we bring the idea of  $F_{ratio}$ , which is determined by the ratio between the frequency difference ( $\Delta f$ ) and the cutoff frequency, namely,  $\Delta f / F_{cutoff}$  from the previous papers [22], [25]. In order to take the nonlinear effect of the diodes into

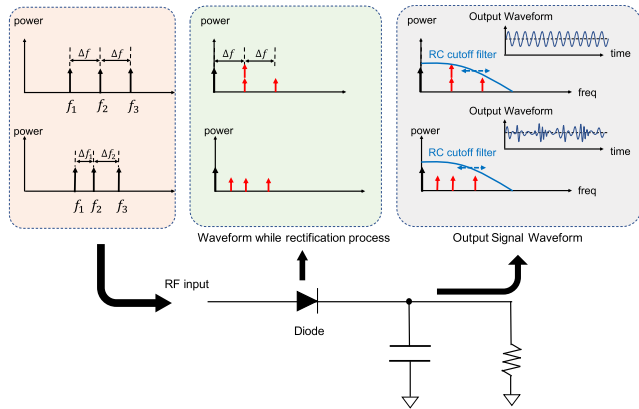


**FIGURE 1.** Explanation of how output voltage changes depending on the tone configurations for the case of  $N = 3$ . Depending on the tone configurations of the input waveforms, intermodulation products of harmonic generated signals vary through the process of rectification. These differences can be observed by measuring the output PAPRs, which results in retrieving information.

account, it is required to compare the cutoff frequency with the IM2 tone that is the farthest, or  $BW = f_N - f_1$ , away from 0 Hz. In that context,  $\Delta f$  in this case needs to be  $BW$ . Therefore,  $F_{ratio}$  is defined as  $BW/F_{cutoff}$  in this paper.

PAPRs are utilized as a way to decode output symbols. Assuming that the output voltage is obtained as  $V_{out}$ , then the PAPRs are obtained based on the following;

$$PAPR = \left\{ \frac{\max(V_{out}(t))}{E(V_{out}(t))} \right\}^2. \quad (8)$$

Note that, usually for obtaining PAPRs, it is required to calculate average powers and peak powers. However, since the output  $V_{out}$  is in the DC region, obtaining the average voltage and the peak voltage first and then calculating the square of peak voltage divided by the average voltage is enough. This may reduce the calculation cost. The behaviors of the voltage transitions from the rectification processes to the output for the case of voltage doubler-type rectifiers are discussed in [25], [26]. However, the realizations of  $V_{out}$  is extremely challenging as the formula with regard to  $V_{out}$  include nonlinear expressions, thus, the behaviors of such equations are analyzed through simulation [5], [9], [25]–[27].

As an example, consider the case of  $N = 3$ , and each tone is located at  $f_1, f_2$ , and  $f_3$ , respectively in the frequency domain. As in Fig. 1 on the top, when the tones were evenly distributed, the frequency spacing between the adjacent tones are the same, namely  $|f_2 - f_1| = |f_3 - f_2| = \Delta f$ . In such a case, the frequency differences of the IM2 in the waveform become multiples of  $\Delta f$ , and the IM2 tones whose frequencies are  $\Delta f$  overlaps in the frequency domain as indicated at the top center in Fig. 1. On the other hand, if the frequency spacings are different from each other, namely  $\Delta f(1, 2) \neq \Delta f(2, 3)$ , then the IM2s scatter in the frequency domain. These differences enable the differentiation of the PAPR values, and hence allow the receiver devices to decode the signal.

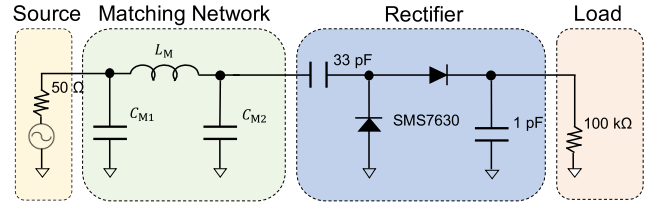


**FIGURE 2.** The tested rectifier circuit for the experiment and simulation. Matching networks for hardware and software are different from each other.

However, these PAPR differences are affected by the RC cutoff frequency. As it can be seen in Fig. 1 at the top right, when the IM2 tones are inside the RC cutoff frequency, all the tones can be seen at the outputs. This results in having varieties of output behaviors. However, when the RC cutoff frequency is too small, the output behaviors between the two examples do not differ with each other. Thus, it is required to properly design the RC filters in order to differentiate the tone configurations based on the outputs.

### C. SIMULATION AND EXPERIMENTAL SETUP

In order to see the PAPR differences caused by changing the tone arrangements of the multitone waveforms and how they differ with the total bandwidth, we conducted simulations and experiments using the rectifier whose circuit diagram is shown in Fig. 2. As for the simulation, we used a harmonic balance simulations from an advanced design system (ADS) circuit simulator.

For the experiments, we implemented the rectifier and directly connected to a signal generator (SMB100A). We measured the output rectified voltage through an oscilloscope (RTO1024) and calculated the PAPR values based on Eq. 8. For the signal generation, the number of tones was set to 3, and the signal bandwidth was fixed to 200 kHz. The carrier frequency was set to 915 MHz. The tone arrangements were  $f_c - \frac{BW}{2}, f_c - \frac{BW}{2} + xBW$ , and  $f_c + \frac{BW}{2}$  respectively, and  $x$  ranged from 0.1 to 0.9. Here,  $f_c$  is the carrier frequency. The rectifier consisted of a matching network, a voltage doubler rectifier, a storage capacitor, and a load resistor. We used this type of rectifier since it is popular among the RF power harvesting community [28]. The diode type was SMS7630-005LF. The capacitance and load resistance were set to 1 pF and 100 kΩ, respectively. We manually optimized the matching network for both simulation and experiment. As for the simulation, we conducted Large-Signal S-Parameter Simulation (LSSP) at 915 MHz frequency and optimized for the input power of  $-10$  dBm. For the real implementation, we used a Vector Network Analyzer (VNA) ZNB20 in order to perform impedance matching.

### D. PRELIMINARY RESULTS

The simulation and experimental results when sweeping the middle tone in the frequency domain of the multitone waveforms were shown in Fig. 3. When the tones are evenly distributed in the frequency domain ( $x = 0.5$ ), the obtained out-

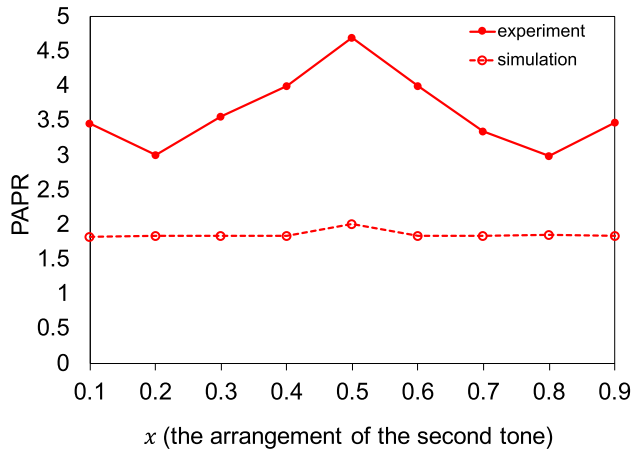


**FIGURE 3.** Simulation and experimental result of PAPR variations using a single rectifier circuit.  $x$  represents the arrangement of the middle tone among the three tones. The number of tones of the multitone signal was 3, the total bandwidth was set to 200 kHz, and the input power was  $-10$  dBm.

**TABLE 1.** PAPR differences for even and uneven tone configurations for  $P_{in} = -10$  dBm and  $BW = 200$  kHz.

	even	uneven (averaged)	uneven (standard deviation)
simulation	2.00	1.83	0.01
experiment	4.69	3.48	0.38

put PAPR became the largest among the other cases for both simulation and experiment. In the experiments, the values of the PAPR values were symmetric around the point of  $x = 0.5$ . This behavior is reasonable because the arrangements of the IM2 tones for  $x = 0.4$  and  $x = 0.6$  are the same, which results in having the same PAPR value. Similarly, the same PAPR value can be produced when  $x = 0.3$  and  $x = 0.7$ , when  $x = 0.2$  and  $x = 0.8$ , and when  $x = 0.1$  and  $x = 0.9$ , respectively. In addition, the reason that the highest PAPR was observed when  $x = 0.5$  is that the output voltage becomes smaller than the other cases when  $F_{ratio}$  is small. In other words, overlapping the IM2 tones result in having smaller output voltage when  $F_{ratio}$  is small. Although the theoretical realization cannot be accomplished in any of the previous papers, this tendency is agreed from the results obtained by simulation from the previous paper [26].

We show the PAPR values for the evenly distributed case and the uneven case in Table 1 when  $P_{in} = -10$  dBm and  $BW = 200$  kHz. Note that we compared the evenly distributed case with the unevenly distributed case that was obtained by averaging the results of 8 cases (from  $x = 0.1$  to  $x = 0.9$ , excluding  $x = 0.5$ ) including the standard deviations. Although the PAPR difference was only 0.17 for the simulation result, that difference became larger in the experiment.

One of the reasons for having different results between simulation and the experiments stems from the differences in the inductor's Q factor in the impedance matching. For the simulation, we assumed that the inductor is ideal. When the inductor is ideal, the Q factor is almost infinite, which results

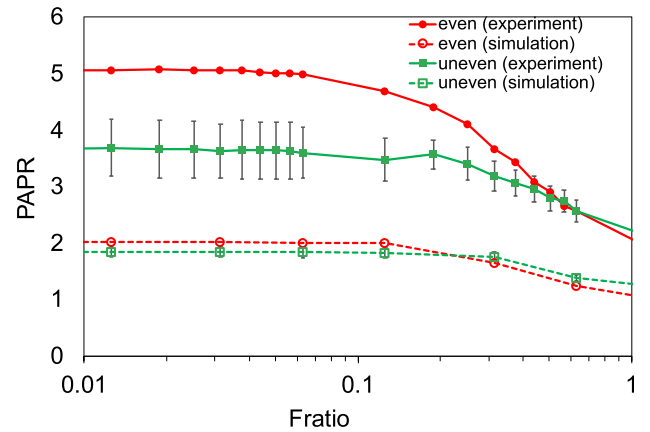


**FIGURE 4.** The simulation and experimental result of output PAPR differences against  $F_{ratio}$  for the single stream rectifier (1 pF and 100k $\Omega$ ).

in narrowing the bandwidth that the rectifier can receive. This indicates that multiple tones that are away from the matched condition (915 MHz) cannot go through the circuit. Therefore, varying the tone configurations has little effect on the output voltage fluctuations, which results in having very similar PAPR values even the tone configurations are different in the simulation. The voltage fluctuations becoming smaller also mean that PAPR values become smaller since the peak power and the average power come close to each other. In contrast, in the experiment, the inductor's Q factor was approximately 70 and even lower when considering the parasitic resistance of the wiring [29]. Therefore, the acceptable bandwidth ( $BW$ ) becomes 13.1 MHz, which is large enough to receive varieties of the multitone waveform in the experiments. This results in having higher PAPR values with larger PAPR differences between  $x = 0.5$  and  $x \neq 0.5$ .

However, this tendency does not hold when the  $F_{ratio}$  becomes large. We plot the simulation and the experimental results of PAPR behavior differences against the  $F_{ratio}$  in Fig. 4. It shows that when  $F_{ratio}$  is higher than 0.2, the PAPR differences for the even and the uneven cases become almost the same, and the relationship is reversed after that for the case of the simulation. The experimental result also shows the same trend, but the threshold value becomes 0.4 instead of 0.2. This shows the limitation of this method. However, in terms of using this method at UHF, where the communication bandwidth only requires 200 kHz, the system does not require a larger  $F_{ratio}$  [18].

Based on the aforementioned discussions, it is required to have the  $F_{ratio}$  to be at most 0.4. Considering that the communication bandwidth requires only up to 200 kHz, under the condition that  $F_{ratio} \leq 0.4$ , the cutoff frequency must be set according to:

$$F_{cutoff} \geq \frac{BW}{0.4}. \tag{9}$$

Therefore, the RC product ( $R_L C_L$ ) needs to be satisfied as;

$$R_L C_L \leq \frac{0.4}{2\pi BW}. \tag{10}$$

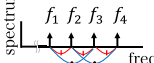
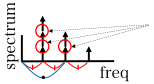
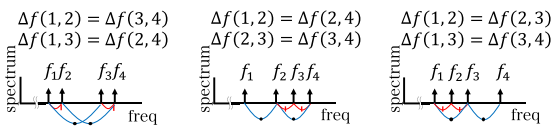
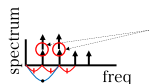
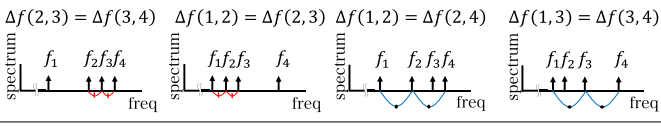
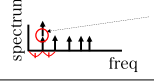
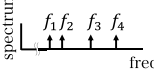
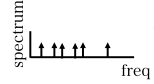
categories	Input waveforms to a receiver	Output waveforms from a receiver
Category A	$\Delta f(1,2) = \Delta f(2,3) = \Delta f(3,4)$ $\Delta f(1,3) = \Delta f(2,4)$ 	
Category B	$\Delta f(1,2) = \Delta f(3,4)$ $\Delta f(1,2) = \Delta f(2,4)$ $\Delta f(1,2) = \Delta f(2,3)$ $\Delta f(1,3) = \Delta f(2,4)$ $\Delta f(2,3) = \Delta f(3,4)$ 	
Category C	$\Delta f(2,3) = \Delta f(3,4)$ $\Delta f(1,2) = \Delta f(2,3)$ $\Delta f(1,2) = \Delta f(2,4)$ $\Delta f(1,3) = \Delta f(3,4)$ 	
Category D		

FIGURE 5. The categories of the tone configurations based on the different PAPR values generated at the output.

When setting the load resistance to be 100 kΩ the capacitance must be smaller than 3.18 pF. In the experiment, the selected 1 pF and 100 kΩ met these criteria.

### III. INFORMATION ENCODING METHOD

From the previous section, we revealed that the differences in PAPRs depend on the number of equal values in the IM2s, which also correspond to how many overlaps occur at the output in the frequency domain. Based on this, we reveal how many different PAPRs can be produced for a given number of tones and what kind of tone variations yield specific PAPRs. The former is needed for estimating the modulation order, which is required to obtain the communication rate. The modulation order  $M$  is defined as the following;

$$M = \log_2\{N_{\text{categories}}\}, \tag{11}$$

where  $N_{\text{categories}}$  is the number of possible different PAPRs to be generated based on the tone arrangements.

#### A. MODULATION ORDER ESTIMATION

##### 1) ESTIMATION OF THE TOTAL NUMBER OF FREQUENCY SPACINGS

When the number of tones are  $N$ ,  $N_{\text{TotalPairs}} = N(N - 1)/2$  numbers of the IM2s are generated, each of which is expressed as  $\Delta f(i, j), \forall i, j \in N, i < j$ . As an example, when  $N$  is 4, the IM2 are  $\Delta f(1, 2), \Delta f(1, 3), \Delta f(1, 4), \Delta f(2, 3), \Delta f(2, 4),$  and  $\Delta f(3, 4)$ . Therefore, there are 6 IM2s to be generated.

##### 2) CATEGORIZATIONS

$N_{\text{TotalPairs}}$  number of IM2 tones generate the varieties of PAPRs depending on the arrangement of the tones in the

waveforms. One of our goal is to categorize the tone configurations of the frequency tones according to PAPR values. This leads to revealing how many different symbols can be produced within the number of tones. In order to correctly formulate the categorizations, we start with an example case to get some insights.

##### a: 4 TONE CASE

When  $N = 4$ , based on an exhaustive search, we can categorize the configurations of the input waveforms to a receiver into 4, as shown in Fig. 5. In Category A, the tone configurations are such that  $\Delta f(1, 2) = \Delta f(2, 3) = \Delta f(3, 4)$  and  $\Delta f(1, 3) = \Delta f(2, 4)$ . This case occurs when all the tones are evenly distributed. There are 3 equals that can be observed when we see the right hand side of Fig. 5, 3 overlaps occur at the output. In Category B, there are two pairs of IM2s corresponding to the two frequency differences. For example, one of the tone combinations is  $\Delta f(1, 2) = \Delta f(3, 4)$  and  $\Delta f(1, 3) = \Delta f(2, 4)$ , but  $\Delta f(1, 3) \neq \Delta f(3, 4)$ . In this case, there are 2 overlaps at the output. In the same way, in Category C, there is only one pair of IM2s that has the same frequency differences, where only 1 overlap happens at the output. Finally, in Category D, each tone does not have the same frequency difference. At the output side, the IM2 tones are scattered around in the frequency domain.

Our key findings are the following. First, the number of equals does not exceed 3 among the pairs of IM2s when  $N = 4$ . Moreover, this 3 consist of 2 equals coming from the adjacent tones ( $\Delta f(1, 2) = \Delta f(2, 3) = \Delta f(3, 4)$ ), and 1 from every other tone ( $\Delta f(1, 3) = \Delta f(2, 4)$ ). No pair is more than two tones apart. In addition, at least on of the tone combinations exists for the case when the number of equals are 0, 1, 2, or 3. Therefore, in total, the number of categories obtained is 4 for  $N = 4$ .

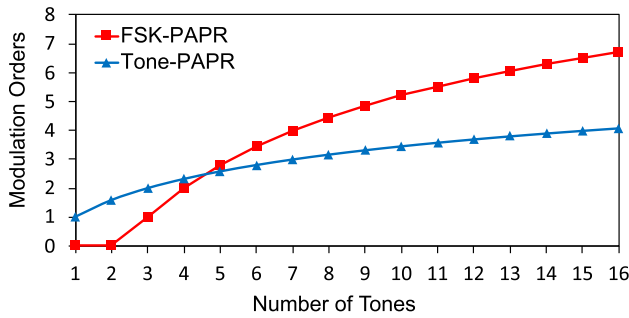


FIGURE 6. The number of tones versus modulation orders; we compared our scheme with the conventional Tone-PAPR based modulation scheme.

**b: GENERAL CASE**

Based on the aforementioned discussions, in the general case, the number of categories can be counted for all the cases when the number of equal values in the IM2 is 0, 1, . . . ,  $N_{EqualNumbers}$ , where  $N_{EqualNumbers}$  is the maximum number of equals that IM2 can produce, which can be achieved when the tones are evenly distributed. Therefore,  $N_{EqualNumbers}$  consists of  $(N - 2)$  equals from the adjacent tones,  $(N - 3)$  equals from every other tone, . . . , 1 equal. Therefore, we can derive  $N_{EqualNumbers} = \frac{(N-1)(N-2)}{2}$ . Overall, the number of categories ( $N_{categories}$ ) is  $N_{EqualNumbers} + 1$  since the number of equal values in the IM2s have either 0, 1, . . . ,  $N_{EqualNumbers}$ . As a result, the modulation order  $M$  can be obtained by the following equation;

$$M = \log_2\{(N - 1)(N - 2)/2 + 1\}. \tag{12}$$

The relationship between the modulation orders with regard to the given  $N$  is shown in Fig. 6. We compared with the conventional modulation scheme based on the number of tones, which is labeled as Tone-PAPR in this figure [20]. Based on this result, our method can reduce the number of tones in order to achieve a higher-order modulation scheme under the condition that  $N \geq 5$ . On the other hand, the previous FSK PAPR method only requires to have different IM2 tone arrangements for obtaining different symbols; the tone configurations can be considered almost infinitely by varying the size of the frequency spacings [22]. Therefore, in terms of modulation order, our scheme is inferior to the previous system.

**B. COMMUNICATION RATE**

Next, we will estimate the communication rate in this section. The communication rate can be obtained by the minimum frequency spacing  $\Delta f_{min}$  among the tones and the modulation order  $M$ . Therefore, we can express in the following;

$$R = \Delta f_{min} \times M. \tag{13}$$

However, revealing  $\Delta f_{min}$  is not trivial since it is required to arrange the tone configuration in the frequency domain, which results in having different frequency spacing among the symbols. In order to analyze  $\Delta f_{min}$ , we introduce two parameters; *Scale* and *factor*. *Scale* constrains the minimum

frequency spacing that adjacent tones can take. The adjacent tones have to be separated by a multiple of  $\Delta f_{scale} = BW/Scale$ . The parameter, *factor*, represents how many times the actual  $\Delta f_{min}$  is multiplied by  $\Delta f_{scale}$  among the transmitting symbols. Therefore, we can express the minimum frequency spacing as follows;

$$\Delta f_{min} = \frac{factor \times BW}{Scale}. \tag{14}$$

Finally, the spectrum efficiency can be determined by the normalized throughput, which is expressed as;

$$S_E = \frac{R}{BW}. \tag{15}$$

Next, we discuss how these parameters relate to each other and we will compare the spectrum efficiencies with the existing methods.

**C. PARAMETER SELECTIONS**

In this section, we will discuss the relation between the communication rate and the choice of *Scale*. If the *Scale* is large, the  $\Delta f_{scale}$  becomes small. Thus, many varieties of the combinations of the IM2s can be considered. However, this results in having a low communication rate as it is rate-limited by the  $\Delta f_{scale}$ . On the other hand, if *Scale* is small, the communication rate becomes faster, but the number of combinations becomes poor, and not all the types of combinations can be obtained. This may render the method unable to convey information in the extreme case.

**1) 4 TONE CASE**

We show the relationship between the *Scale* and the tone placement in Fig. 7. As we see from the figure, increasing the *Scale* results in having small  $\Delta f_{scale}$  and eventually having small  $\Delta f_{min}$ . However, the number of tone arrangements increases since the number of indices that the second and the third tone can choose increases. Note that the 1st and the last tone are always placed at each end, separated by  $BW$  and cannot be arranged in other places. In Fig. 7, all the cases represent  $\Delta f(1, 2) = \Delta f(3, 4) \wedge \Delta f(1, 3) = \Delta f(2, 4)$ , for each *Scale* as an example.

When the *Scale* is 4, the  $f_{scale}$  becomes  $BW/4$ , so the communication rate is increased as the  $f_{min}$  increases. However, in such a case, all the possible candidate tone configurations are reduced to only 3: (0, 1, 3, 4), (0, 1, 2, 4), and (0, 2, 3, 4) whose types of the tone configurations are  $\Delta f(1, 2) = \Delta f(3, 4) \wedge \Delta f(1, 3) = \Delta f(2, 4)$ ,  $\Delta f(1, 2) = \Delta f(2, 3) \wedge \Delta f(1, 3) = \Delta f(3, 4)$ , and  $\Delta f(2, 3) = \Delta f(3, 4) \wedge \Delta f(1, 2) = \Delta f(2, 4)$ , respectively. Note here that each element stands for the index in the frequency domain in Fig. 7. Since these types of the tone configurations all belong to Category B, we cannot send a bit of information in this case because all the outputs fall into the same value without being differentiated.

On the other hand, when the *Scale* is 12,  $\Delta f_{scale}$  becomes  $BW/12$ . Therefore, the tone combinations increase significantly. As we see from Fig. 7 at the bottom, there are 11 places

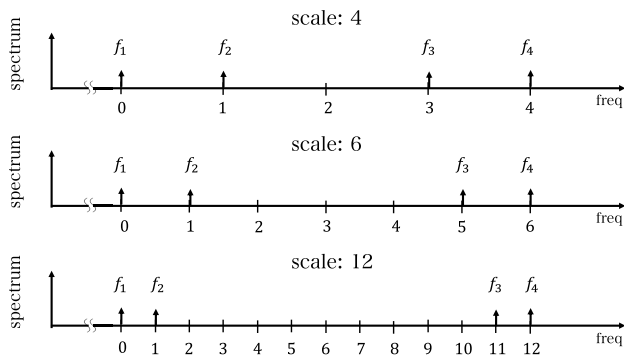


**FIGURE 7.** Scale explanation. As the number of scale increases, the minimum frequency spacing between the adjacent tones decreases.

**TABLE 2.** The number of types of the tone configurations which is shown in Fig. 5, and the number of possible candidate tone configurations for the case of  $N = 4$  (Scale = 12).

categories	Number of Types of tone configurations	Number of possible tone configurations
Category A	1	34
Category B	4	14
Category C	3	6
Category D	1	1

for the second and third tones to be arranged (indexes 1 to 11). Note that the 1st and the last tones are always placed at each end, separated by  $BW$  and cannot be arranged in other places. We show the number of tone configurations for each category in Table 2. From the table, there are 34, 14, 6, and 1 possible tone configurations of the frequency tones that belong to categories A, B, C, and D, respectively. The 14 possible tone configurations in the Category B yield the same PAPR values, and they are categorized into 4 types, as shown in Fig 5.

At the same time, the number of tone configurations that belong to the same types is also increased. These tone configurations include different *factor*. We show the example of the case of different tone arrangements whose types of tone configurations ( $\Delta f(1, 2) = \Delta f(3, 4) \wedge \Delta f(2, 4) = \Delta f(1, 3)$ ) are all the same in Fig. 8. As in Fig. 8, there are 4 different tone configurations to be considered ((0, 5, 7, 12), (0, 3, 9, 12), (0, 2, 10, 12), and (0, 1, 11, 12)). Note that (0, 4, 8, 12) is in Category A because all the tones are evenly distributed, so this case is omitted. Any of these tones fall into the Category B. The differences are that they have different *factors*, which are 2, 3, 2, and 1, respectively. In order to obtain a faster communication rate,  $\Delta f_{\min}$  needs to be large. In that perspective, (0, 3, 9, 12) is the tone configuration whose minimum frequency spacing is the largest. The maximum value of *factor* differs from the categories. Based on our brute force search, we found the values of maximum *factors* for each category as 4, 3, 2, and 3 from categories A to D respectively. Since the communication rate is rate-limited to the slowest  $f_{\min}$ , the communication rate for the case of this example becomes,  $R = \log_2(4) \times \frac{2 \times BW}{12} = \frac{BW}{3}$ . Here, since

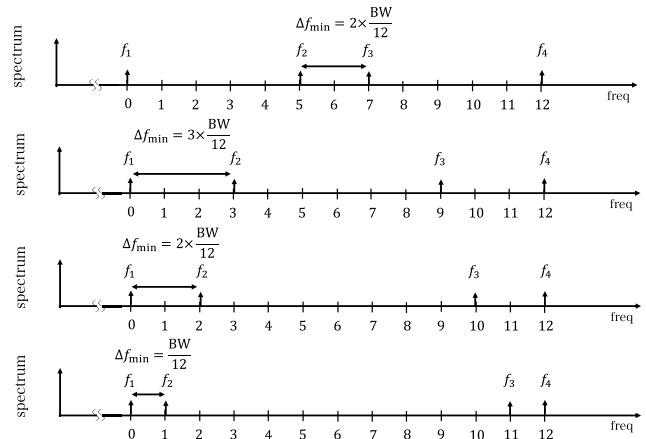


**FIGURE 8.** Tone selection differences and how the minimum frequency spacings differ are shown. All the combinations represent the case of  $\Delta f(1, 2) = \Delta f(3, 4) \wedge \Delta f(1, 3) = \Delta f(2, 4)$ , but the minimum frequency spacings ( $\Delta f_{\min}$ ) are different depending on the tone configurations.

**TABLE 3.** Relations of  $\Delta f_{\text{scale}}$ , *factor*,  $\Delta f_{\min}$  for different  $N$ .

N	3	4	5	6	7
# of possible PAPRs	2	4	7	11	16
$\Delta f_{\text{scale}}$	$\frac{BW}{4}$	$\frac{BW}{6}$	$\frac{BW}{12}$	$\frac{BW}{30}$	$\frac{BW}{48}$
<i>factor</i>	1	1	1	4	5
$\Delta f_{\min}$	$\frac{BW}{4}$	$\frac{BW}{6}$	$\frac{BW}{12}$	$\frac{2BW}{15}$	$\frac{5BW}{48}$

4 categories exist for this example, the modulation order is obtained as  $M = \log_2(4)$ .

The optimal case can be defined as the minimum *Scale* that at least one candidate set exists for each category, which in this case, *Scale* = 6. In such a case, the number of types for each category is 1, 1, 6, and 2 from categories A to D respectively. By reducing the *Scale*, it is possible to find candidate tone configurations for symbols with smaller search space as well. The total candidate tone configurations are reduced to 10 from 55 when the scale is 12.

## 2) LARGER NUMBER OF TONES

Obtaining a suitable *Scale* analytically for a given number of  $N$  is difficult. Therefore, we solved this by brute force search. We tested with a small value to see if the candidate tone configurations included all the categories. Based on the brute force search, we obtained the  $\Delta f_{\text{scale}}$ ,  $\Delta f_{\text{factor}}$ , and  $\Delta f_{\min}$  for different  $N$  from 3 up to 7, which is shown in Table 3. Since increasing the number of  $N$  requires a huge search space, we were unable to find a suitable *Scale* for  $N > 7$  due to the limitation of computational resources. As can be seen, up to  $N = 5$ , *factor* becomes 1, which means that there exist at least one category whose *factor* is 1. On the other hand, for  $N > 5$ , the minimum *scale* becomes 4 for  $N = 6$ , and 5 for  $N = 7$ , which indicates that by carefully choosing the specific tone



TABLE 4. The tone features depending on the categories for  $N = 3$  and  $Scale = 4$ .

	types of tone configurations	the number of equals	factors	number of configurations	candidate configurations
Category A	$\Delta f(1, 2) = \Delta f(2, 3)$	1	2	1	(0, 2, 4).
Category B	no features	0	1	2	(0, 1, 4), (0, 3, 4).

TABLE 5. The tone features depending on the categories for  $N = 4$  and  $Scale = 6$ .

	types of tone configurations	the number of equals	factors	number of configurations	candidate configurations
Category A	$\Delta f(1, 2) = \Delta f(2, 3) = \Delta f(3, 4) \wedge$ $\Delta f(1, 3) = \Delta f(2, 4)$	3	2	1	(0, 2, 4, 6).
Category B	$\Delta f(1, 2) = \Delta f(3, 4) \wedge \Delta f(1, 3) = \Delta f(2, 4)$	2	1	1	(0, 1, 5, 6).
Category C	$\Delta f(1, 2) = \Delta f(2, 3) \vee$ $\Delta f(1, 2) = \Delta f(2, 4) \vee$ $\Delta f(1, 3) = \Delta f(3, 4) \vee$ $\Delta f(2, 3) = \Delta f(3, 4)$	1	1	6	(0, 1, 2, 6), (0, 1, 3, 6), (0, 2, 3, 6), (0, 3, 4, 6), (0, 3, 5, 6), (0, 4, 5, 6).
Category D	No features	0	1	2	(0, 1, 4, 6), (0, 2, 5, 6).

TABLE 6. The tone features depending on the categories for  $N = 5$  and  $Scale = 12$ .

	types of tone configurations	the number of equals	factors	number of configurations	candidate configurations
Category A	$\Delta f(1, 2) = \Delta f(2, 3) = \Delta f(3, 4) = \Delta f(4, 5) \wedge$ $\Delta f(1, 3) = \Delta f(2, 4) = \Delta f(3, 5) \wedge$ $\Delta f(1, 4) = \Delta f(2, 5)$	6	3	1	(0, 3, 6, 9, 12).
Category B	$\Delta f(1, 2) = \Delta f(2, 4) = \Delta f(4, 5) \wedge$ $\Delta f(1, 3) = \Delta f(3, 5) \wedge$ $\Delta f(1, 4) = \Delta f(2, 5) \wedge$ $\Delta f(2, 3) = \Delta f(3, 4)$	5	2	1	(0, 4, 6, 8, 12).
Category C	$\Delta f(1, 2) = \Delta f(2, 3) = \Delta f(3, 4) \wedge$ $\Delta f(1, 3) = \Delta f(2, 4) \wedge$ $\Delta f(1, 4) = \Delta f(4, 5)$ , ...	4	2	11	(0, 2, 4, 6, 12), (0, 4, 6, 10, 12), (0, 6, 8, 10, 12) ..., (8 more).
Category D	$\Delta f(1, 2) = \Delta f(4, 5) \wedge$ $\Delta f(1, 4) = \Delta f(2, 5) \wedge$ $\Delta f(1, 3) = \Delta f(3, 4)$ , ...	3	2	6	(0, 2, 5, 10, 12), (0, 3, 5, 7, 12), (0, 5, 7, 9, 12), ... (3 more)
Category E	$\Delta f(1, 2) = \Delta f(2, 3) \wedge$ $\Delta f(2, 4) = \Delta f(4, 5)$ , ...	2	2	12	(0, 2, 4, 7, 12), (0, 3, 5, 8, 12), ..., (10 more)
Category F	$\Delta f(1, 2) = \Delta f(2, 3) \vee$ $\Delta f(2, 3) = \Delta f(3, 4) \vee$ $\Delta f(3, 4) = \Delta f(4, 5) \vee$ $\Delta f(2, 3) = \Delta f(3, 4) \vee$	1	2	4	(0, 2, 4, 9, 12), (0, 2, 5, 8, 12), (0, 3, 8, 10, 12), (0, 4, 7, 10, 12).
Category G	no features	0	1	14	(0, 1, 3, 7, 12), ... (13 more).

combinations, it is possible to have the tone combinations that can increase the communication rate.

We show the detailed results for the case of  $N = 3$ ,  $N = 4$ , and  $N = 5$  in Table 4 – Table 6. In the tables, we show the types of tone configurations, the number of equals, the largest factor among the tone configurations, the number of combinations, and the actual candidate set examples that resulted the fastest for each category. These results were obtained by considering all the possible cases and categorizing them analytically. Note that for  $N = 5$ , there are a lot of types to be considered, so we show only part of the results. Each factor in Table 4 – Table 6 is the factor within the categories and the factor that is listed in Table 3 is the minimum value among categories. This is because the minimum value of the factor among the categories is rate-limited in terms of communication rate.

We compared the spectrum efficiency with the most related papers in Fig. 9, which shows that our case achieves the poorest performances. The spectrum efficiencies of the other schemes were calculated based on the results in their papers [20], [22]. The spectral efficiency becomes 4 times smaller than the conventional multitone FSK method. In addition, we see that there is a slight degradation against PAPR based multitone SWIPT as well when  $N$  is a small value. However, as the number of tones is increased, the efficiency improves and comes close to the multitone-PAPR method. In fact, as shown in Fig. 6, increasing the number of tones results in having a larger modulation order than the multitone-PAPR case. Therefore, for a larger  $N$ , we could obtain a better performance against the multitone-PAPR method. Note that our scheme stands for the fastest configuration whose tone combinations are selected from Table 4 – 6.

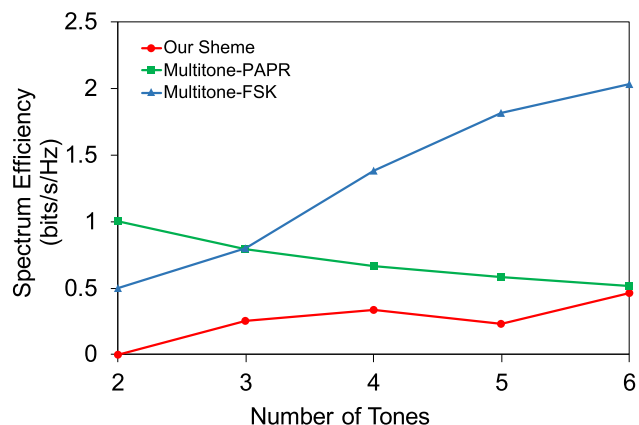


FIGURE 9. Spectrum efficiency comparison; These results are referred from the results of previous papers.

Finally, we discuss the difference between the aforementioned tone selections and the previously published multitone FSK SWIPT method [22]. As opposed to the conventional method where the tones are selected so that each IM2 from the tone combinations are different, our method selects the combinations of tone configurations whose numbers of equal values in the IM2s generated from the combinations, are different. Borrowing the expressions from [22], the tone combinations include both uniform and nonuniform multitone FSK, which is also one of the differences. While the previous paper reports the possibility to consider more varieties of selections, we constrained the total bandwidth to be the same in order to make the choice of tone selection easier. This results in degrading the spectral efficiency.

#### IV. DESIGN RECEIVER SYSTEM AND SIMULATION VALIDATIONS

Based on our previous results, we were able to encode bits based on the frequency tone arrangements. In this section, we validate our method using the SWIPT receiver, which consists of both information decoding units and the energy harvesting unit. Our design requirement is that the SWIPT receiver should both receive RF energy harvesting power and RF signal simultaneously using the same antenna. In addition, we assumed that the receiver circuit has very low power computational resources.

##### A. RECEIVER SYSTEM MODEL

The block diagram of the tested rectifier circuit to achieve SWIPT is shown in Fig. 10. It consists of two units; the first unit is for obtaining RF energy, which works as a battery source for the receiver circuit. The second rectifier unit works for obtaining PAPR by observing the peak voltage and the averaged voltage. We connected these units after the matching network. Note that by changing the DC block capacitors for each unit, we would change the RF input power so that more power may flow into the energy harvesting unit [30]. We will refer to this two-unit type rectifier as

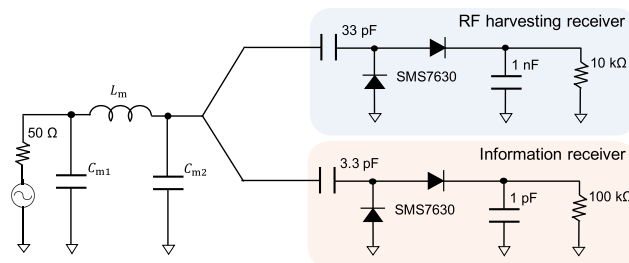


FIGURE 10. The circuit model for ADS circuit simulation and experiment. The impedance was matched using an optimization tool in ADS. The received signal is split into two units; one is for the RF harvesting receiver (top), and the other is for calculating PAPRs. Both of the modules consists of passive elements.

a 2 stream rectifier and the rectifier design shown in Fig. 2 as a single-stream rectifier in later discussions.

##### B. PAPR MEASUREMENT VALIDATION

We conducted simulations and experiments in order to see if the presented receiver circuit could successfully distinguish PAPR differences based on the previously showed signal generation method. The simulation and experiment setup is the same as that described in section II-C. Note that the impedance matching was optimized to  $-10$  dBm and did not rematch even with different input power since in a usual receiver system, changing the matching network depending on its input power is not practical.

##### 1) PAPR PERFORMANCE CHARACTERIZATION AGAINST INPUT POWER

For the tone selections, we utilized some of the tones from Table 4 - Table 6. If the candidate sets included multiple sets, we averaged the output PAPR of all the tested cases. The input power was set to  $-10$  dBm, the communication bandwidth was fixed to 200 kHz, and the center frequency was set to 915 MHz. The output PAPR was derived based on the Eq. 8. We show the simulation and experimental results in Fig. 11 and Fig. 12 for  $N = 3$  and 4. Both experimental and simulation results show that we were able to distinguish  $(N - 1)(N - 2)/2 + 1$  different combinations. However, for the experimental results, the PAPR value became unstable for power lower than  $-18$  dBm. When the obtained output voltage was too small and the obtained peak voltage was relatively high, the peak to average power raised significantly. This resulted in unstable PAPRs when the low input powers were induced. Therefore, it is hard to use in practice for such small input power. In spite of this result, the typical energy harvesting receiver commercially available requires more than  $-12$  dBm input power for its operation, so operating above  $-18$  dBm is feasible for practical use [31].

Another thing to express is that the PAPR values change depending on the input power level within the same category. This means that even if the receiver device obtains a specific PAPR value, it cannot correctly identify which category it is in. For example, when the receiver device receives the  $N = 4$  tone waveforms and receives output PAPR that is

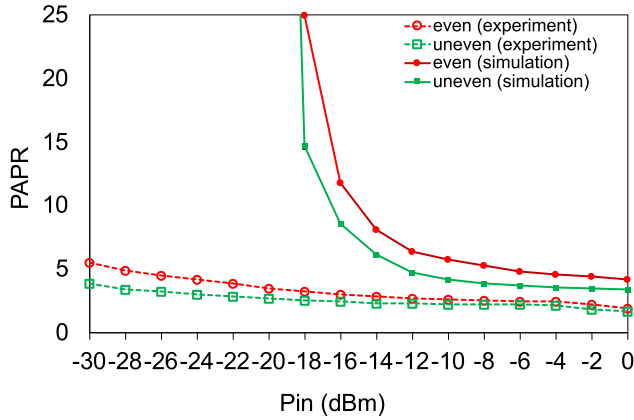


FIGURE 11. Simulation results of PAPR comparison based on the categories in Table 4 for  $N = 3$  with the introduced receiver circuit.

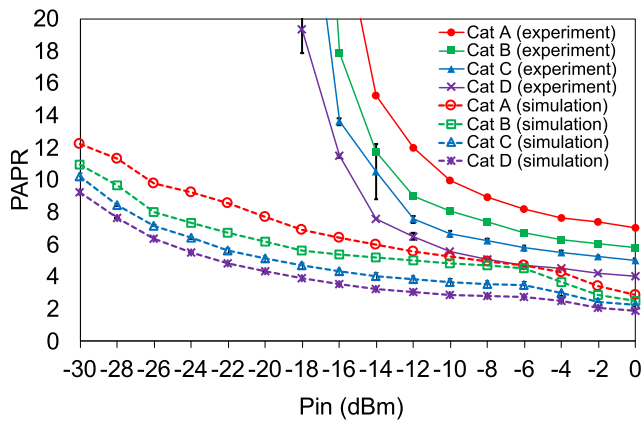


FIGURE 12. Simulation and experimental results of PAPR comparison based on the categories in Table 5 for  $N = 4$ .

indicated as 8, the system cannot decide which category does the tone configuration of the transmitted waveforms belongs to unless the receiver device obtained received power as well. This occurs because Category A with input power  $-6$  dBm, Category B with input power  $-10$  dBm, Category C with input power  $-12.2$  dBm, and Category D with input power  $-14.1$  dBm all output PAPR values of 8. Therefore, in order to utilize this scheme, it is required to have an initial reference signal used to measure the received power at the receiver node. Simply put, the transmitter device sends the preambles of all the categories at first so that the receiver can understand the mapping between the PAPR values and the categories. One might say that input power level changes depending on the timing of the transmitted signal. However, in a case where the transmitter and receiver nodes are in fixed places, the input power level would not change unless the wireless channel changes dramatically, like in an urban city. Therefore, assuming that in a rural area, where the wireless channel would not change dramatically, we could assume that the wireless channel might be fixed for a short period of time, which is enough time for the receiver node to receive information.

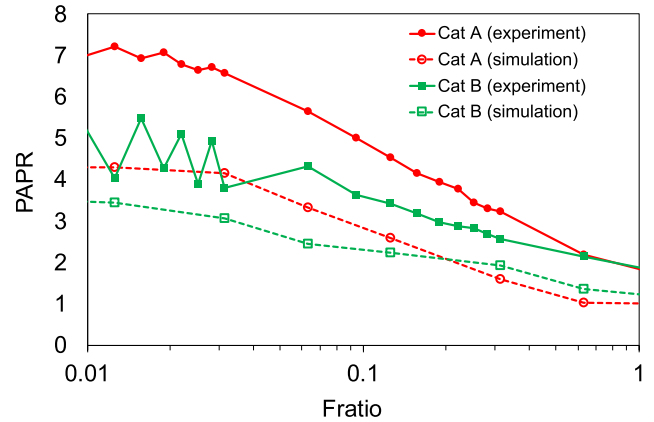


FIGURE 13. Simulation and experimental results of PAPR comparisons against  $F_{ratio}$  for  $N = 3$ . The tested rectifier was the 2 stream rectifier that is shown in Fig. 10 and the BW was varied from 10 kHz to 1 MHz. The input power was set to  $-10$  dBm.

### 2) PAPR PERFORMANCE CHARACTERIZATION AGAINST $F_{ratio}$

We further investigate the PAPR difference against  $F_{ratio}$  for the case of  $N = 3$ , whose result is shown in Fig. 13. The tested receiver circuit is the same as in Fig. 10. We varied the bandwidth from 10 kHz to 1 MHz, which corresponds to  $F_{ratio}$  of 0.01 to 1. From Fig. 13, the PAPR difference between the categories A and B in Table 4 becomes smaller for larger  $F_{ratio}$ . When larger bandwidth is allocated, the generated IM2s are more likely to go beyond the  $F_{ratio}$  in the frequency domain, which results in having smaller alternative current (AC) components in the output voltage. Therefore, the output voltage fluctuation between the categories resembles each other. That is to say, our system fails to retrieve information for a larger bandwidth or a lower RC factor, which resembles the results from a single-stream rectifier in Fig. 4. Note that we are assuming the use of this system to be for the UHF regime. In such a regime, the required bandwidth is at most 200 kHz, which is relatively small. As we discussed in section II-D, even though our method works with a small  $F_{ratio}$  regime, our method is enough for operating at UHF. On the other hand, when we consider using this method to the system where the communication bandwidth can be much larger than our assumption, our method is not suitable for adoption. In such scenarios, the previously published method is beneficial for information retrieving [22].

### 3) PAPR PERFORMANCE CHARACTERIZATION AGAINST $F_{ratio}$

Finally, we compare the output voltage acquisitions of the main RF harvesting unit. The experimental result of the output voltage from the main RF harvesting unit of the 2 stream type rectifier is shown in Fig. 14. In addition, we compare it with the single-stream type rectifier shown in Fig. 3, whose load resistance and capacitance were 10 k $\Omega$ , and 1 nF for  $N = 3$ . The input power was set to  $-10$  dBm, and bandwidth was varied from 10 kHz to 1 MHz. In terms of  $F_{ratio}$ , it corresponded to 0.6 to 62. This range is different from the aforementioned analysis due to the fact that the  $\Delta f_{cutoff}$  is different

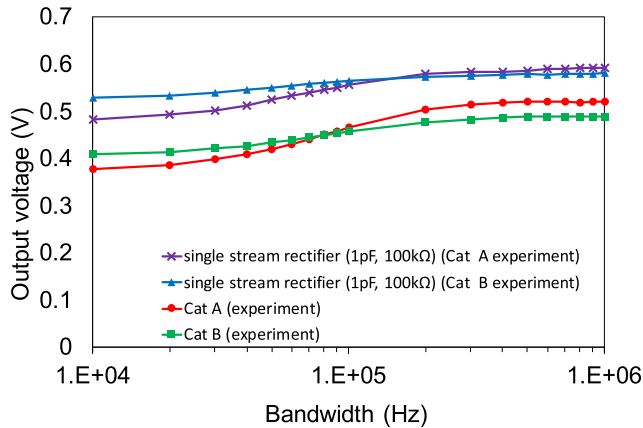


**FIGURE 14.** Experimental results of output voltage comparisons against bandwidth for  $N = 3$ . The tested rectifier was the 2 stream rectifier that is shown in Fig. 10, and the output voltage was inspected from the main RF unit. We also tested a single rectifier circuit whose load resistance was 1 nF and 10 k $\Omega$ . The tested bandwidth was varied from 10 kHz to 1 MHz, and input power was set to  $-10$  dBm.

from those at the information unit. The experimental results show that increasing the bandwidth to some extent results in having higher output voltages in both the 2 stream rectifier case and the single-stream case. When higher bandwidth is allocated, the ripple of the output voltage ceases due to the RC filter effect, resulting in higher output voltages. On the other hand, when the bandwidth is small, the RC filter cannot cutoff the IM2 tones. In such case, the output voltage drops significantly during the negative half cycle of the waveforms, which causes the degradation of WPT performances especially for the case of a voltage doubler rectifier [26]. Comparing the single stream and the 2 streams case, the single-stream case rectifier yields better output voltage performance. This is due to the loss caused by separating the transmission line to the information unit, which consumes some amount of power.

Furthermore, the experiments show that the output voltages for the case of categories A and B flip when higher bandwidth is allocated. This shows that for evenly distributed cases (Category A) when the cutoff frequency cannot slice IM2 tones, severe performance degradation occurs at the output voltage. It is also indicated that when the tones are unevenly distributed, even with the RC filter cutoff AC component of the output voltage, the yielded output voltage cannot improve similarly to the evenly distributed case. This corresponds to the fact that evenly distributed multitone waveforms can maximize the output voltage [32]. Our results reveal that multitone waveforms with evenly distributed waveforms always yield the highest output voltage under the conditions that allocated bandwidth must be large enough. Investigating the tradeoff between the bandwidth and the tone arrangements is our future works since it is out of the scope of this paper.

We also compare the output voltage for the case when  $N = 4$  in Fig. 15, which behaves similarly to the case

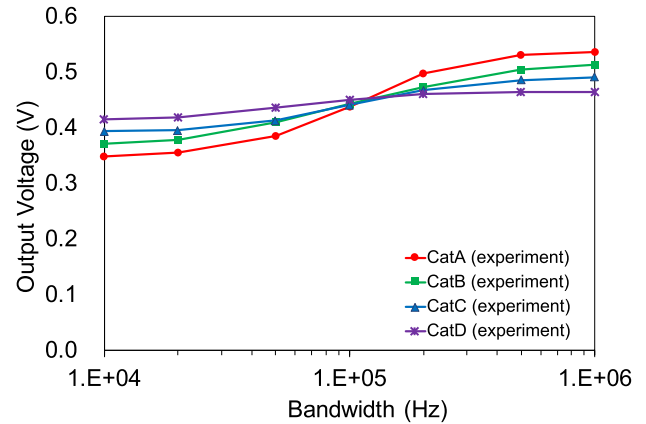


**FIGURE 15.** Experimental results of output voltage comparisons against bandwidth for  $N = 4$ . The tested rectifier was the 2 stream rectifier that is shown in Fig. 10, and the output voltage was inspected from the main RF unit. The tested bandwidth was varied from 10 kHz to 1 MHz, and input power was set to  $-10$  dBm.

when  $N = 3$ . Increasing the number of tones results in having larger differences in terms of the voltage acquisition results from categories A and D, except for the case when the bandwidth reaches 100 kHz. It also shows that on one hand, it is required to allocate larger bandwidth or higher  $F_{\text{ratio}}$ , but on the other hand, in order to get better communication performance,  $F_{\text{ratio}}$  should be small enough to distinguish the PAPR difference between the categories, which is also indicated in previous papers [11], [22]. Thus,  $F_{\text{cutoff}}$  needs to be designed properly for both the RF harvesting unit and the information unit. Finally, in Fig. 16 we show the results for different input power. The bandwidth was set to 200 kHz. As we see from the result, by increasing the input power results in larger differences between the categories in terms of output voltages.

### C. OPTIMIZATIONS

In the previous paper, due to the design of the receiver circuit, when the low-pass-filter (LP-filter) is very narrow, the IM2s in the transmitted tones that reside far away from the DC region are attenuated. This results in detection errors because some of the tones are missed while detecting in the frequency domain. In order to tackle this problem, the previous paper [22], has dealt with pre and post optimizations, which are done at the transmitter and receiver side, respectively. These optimizations are executed based on the knowledge of the transfer function of the LP-filter at the receiver circuit and by multiplying the scaling factor of the waveforms.

In our system, it may be possible to implement such optimizations at both sides, but these optimizations suppress the communication rate eventually. This is because we fix the entire communication bandwidth for each tone configuration in order to make the system easier to select tones. As a result, the furthest IM2 tone generated from the candidate set is  $BW$  away from the DC region. If the  $BW$  happens to be larger than  $F_{\text{cutoff}}$ , signal detection errors will be prone to occur. In such

TABLE 7. Performance summary.

Method	Efficiency	Input power range	carrier frequency	number of tones	calculation cost (summation, multiplication)
Multitone PAPR [20], [21]	8% to 14% at $-10$ dBm	$-20$ dBm to $15$ dBm	900 MHz	4	$O(N)$ , $O(N)$
Multitone FSK [22]	7% to 9% at $-5$ dBm	$-30$ dBm to $0$ dBm	2.45 GHz	4	$O(N \log N)$ , $O(N \log N)$
Biased ASK [18]	22% to 28% at $-15$ dBm	$-25$ dBm to $-5$ dBm	2.45 GHz	2	$O(N)$ , $O(1)$
Amplitude / Phase [11]	46% to 52% at $-10$ dBm	$-20$ dBm to $-6$ dBm	650 MHz to 1 GHz	2	$O(N)$ , $O(1)$
This work	21% to 25% at $-10$ dBm	$-20$ dBm to $0$ dBm	915 MHz	4	$O(N)$ , $O(1)$

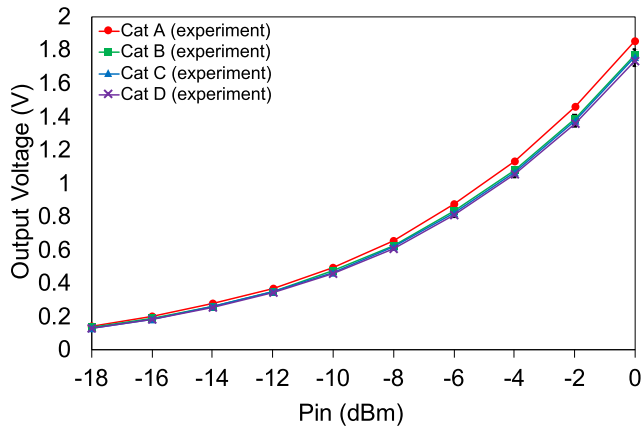


FIGURE 16. Experimental results of output voltage comparisons against input power for  $N = 4$ . The input power was varied from  $-18$  to  $0$  dBm, and the bandwidth was set to 200 kHz. The tested rectifier was the 2 stream rectifier that is shown in Fig. 10, and the output voltage was inspected from the main RF unit.

a scenario, either  $BW$  or  $F_{\text{cutoff}}$  needs to be controlled so that  $BW$  becomes smaller than  $F_{\text{cutoff}}$ . Since the circuit parameter is not easily controlled,  $BW$  needs to be small. This results in degrading the communication rate.

Overall, in the perspectives of the pre and post optimizations, our system has less flexibility compared to the conventional FSK method due to the adoption of fixed bandwidth for tone selections. Finding a method to select tones from unfixed bandwidth conditions might be our future research direction.

## V. DISCUSSIONS

Overall, we have investigated the PAPR detection based multitone FSK. In this section we discuss the comparison with the conventional methods and the feasibility of optimizations that have been discussed in [22].

The advantage of our method relies on the fact that we eliminate the FFT calculation and rely on a PAPR based method performed on the time domain. Typically, the calculation cost of FFT requires  $O(N \log N)$  for multiplications and summations while the PAPR based calculation requires  $O(1)$  for multiplications and  $O(N)$  for summations using the big-O notation. Therefore, in terms of the calculation cost, it is more applicable for a battery-less device. As we also discussed in the introduction, the conventional method can implement passive filter banks in order to avoid the calculation of FFT to obtain information [22]. However, when we implement at UHF where the communication bandwidth lies typically below 1 MHz, it is hard to make a filter that can separate

tones whose frequency spacing is around 1 MHz due to the requirement of a high Q factor. Therefore, even under the uniform FSK case, it is quite challenging to design such filters. It is also possible to implement the filter after the rectification process. However, in such case, the system must embed roughly the same amount of filters as the symbol index. Therefore, trade-off between the size of the receiver circuit and the modulation order needs to be considered. On the other hand, there are also disadvantages from the perspectives of interference or flexibility against the structures.

In terms of interference duration, the conventional method can post compensate the channel effect as they have shown by calculating and negating the channel effect. In addition, in the former paper, signals can be detected even with a small input power (typically around  $-30$  dBm receive power) since it can inspect the spectrum using FFTs [22]. On the other hand in our system, based on the results,  $-18$  dBm received power level is the minimum threshold for the device to correctly detect signals even under the non-interfered condition. Therefore, we conclude that under interference, our system is inferior to the conventional method. Note that the same discussion could be made for noise duration. However, typically, the microwave power transfer signal is significantly above the noise level, so this infers that there is no difference between the method in terms of noise.

As we discussed in the previous section, the conventional method is more flexible with regard to the receiver structure since their method can pre or post optimize the waveform depending on the LP-filter at the receiver side. In order to select tone configurations more simply, we fixed the total bandwidth for each condition which in turn hinders optimization. Even though we could do pre-optimization so as not to be affected by the LP-filter, the communication rate deteriorates severely due to this operation.

Finally, we compared the performances with existing papers [11], [18], [20]–[22] in Table 7. The calculated values are based on the reported results in each paper. Compared with the Multitone FSK, the computational cost is significantly reduced which result from eliminating the calculation of FFT and utilizing PAPR measurement [22]. In addition, we were also able to reduce the calculation complexity against conventional multitone PAPR method. The conventional method calculates average power in order to obtain PAPRs whereas in our case, we only need to measure average output voltage and calculate the power after that, which indicates that multiplication occurs only one time per symbol for obtaining average power [21]. Although modulation based

on amplitude or phase controlling method [11] gained the highest efficiency, the modulation method is too complex to be employed for  $N > 3$ . In our case, the efficiencies varies from 21% to 25% for the case when the number of tones were 4 and the input power range varied from  $-20$  dBm to 0 dBm, which is feasible as we discussed in section. IV-B1.

## VI. CONCLUSION

In this paper, a frequency shift-type multitone signal SWIPT system based on the PAPR detection method is introduced. Different from FFT based signal detection, our method realizes signal detection more simply. We revealed that when the tones vary, the contents of frequency tones in the output voltage varies due to the diode's nonlinearity. In addition, we formulated the relation between the number of tones and the modulation orders and verified it using ADS circuit simulation as well as experiments with our introduced receiver circuit. Based on the results, we could distinguish the  $\frac{(N-1)(N-2)}{2} + 1$  different PAPRs for  $N = 3$ , and  $N = 4$ , which corresponded to our formula. The limitation of our method is with power values under  $-18$  dBm, the PAPR differences are no longer detected. In terms of the theoretical realizations, it is challenging to reveal the output behavior of the rectifier because of the existence of the nonlinear elements. Therefore, the theoretical realizations of output voltage transitions and the PAPRs become our future works.

## ACKNOWLEDGMENT

The authors would like to thank Honorary Professor Tohru Asami for helpful comments.

## REFERENCES

- [1] M. Giordani, M. Polese, M. Mezzavilla, S. Rangan, and M. Zorzi, "Toward 6G networks: Use cases and technologies," *IEEE Commun. Mag.*, vol. 58, no. 3, pp. 55–61, Mar. 2020.
- [2] M. Weiser, "The computer for the 21st century," *Sci. Amer.*, vol. 265, no. 3, pp. 66–75, 1991. [Online]. Available: <http://www.ubiq.com/hypertext/weiser/SciAmDraft3.html>
- [3] I. Krikidis, S. Timotheou, S. Nikolaou, G. Zheng, D. W. K. Ng, and R. Schober, "Simultaneous wireless information and power transfer in modern communication systems," *IEEE Commun. Mag.*, vol. 52, no. 11, pp. 104–110, Nov. 2014.
- [4] T. D. Ponnimbaduge Perera, D. N. K. Jayakody, S. K. Sharma, S. Chatzinotas, and J. Li, "Simultaneous wireless information and power transfer (SWIPT): Recent advances and future challenges," *IEEE Commun. Surveys Tuts.*, vol. 20, no. 1, pp. 264–302, 1st Quart., 2018.
- [5] B. Clerckx, "Wireless information and power transfer: Nonlinearity, waveform design, and rate-energy tradeoff," *IEEE Trans. Signal Process.*, vol. 66, no. 4, pp. 847–862, Feb. 2018.
- [6] Z. Hu, C. Yuan, and F. Gao, "Maximizing harvested energy for full-duplex SWIPT system with power splitting," *IEEE Access*, vol. 5, pp. 24975–24987, 2017.
- [7] R. Jiang, K. Xiong, P. Fan, Y. Zhang, and Z. Zhong, "Optimal design of SWIPT systems with multiple heterogeneous users under non-linear energy harvesting model," *IEEE Access*, vol. 5, pp. 11479–11489, 2017.
- [8] Z. Hu, N. Wei, and Z. Zhang, "Optimal resource allocation for harvested energy maximization in wideband cognitive radio network with SWIPT," *IEEE Access*, vol. 5, pp. 23383–23394, 2017.
- [9] B. Clerckx, R. Zhang, R. Schober, D. W. K. Ng, D. I. Kim, and H. V. Poor, "Fundamentals of wireless information and power transfer: From RF energy harvester models to signal and system designs," *IEEE J. Sel. Areas Commun.*, vol. 37, no. 1, pp. 4–33, Jan. 2019.
- [10] E. Boshkovska, D. W. K. Ng, N. Zlatanov, and R. Schober, "Practical non-linear energy harvesting model and resource allocation for SWIPT systems," *IEEE Commun. Lett.*, vol. 19, no. 12, pp. 2082–2085, Dec. 2015.
- [11] M. Rajabi, N. Pan, S. Claessens, S. Pollin, and D. Schreurs, "Modulation techniques for simultaneous wireless information and power transfer with an integrated rectifier-receiver," *IEEE Trans. Microw. Theory Techn.*, vol. 66, no. 5, pp. 2373–2385, May 2018.
- [12] E. Bayguzina and B. Clerckx, "Asymmetric modulation design for wireless information and power transfer with nonlinear energy harvesting," *IEEE Trans. Wireless Commun.*, vol. 18, no. 12, pp. 5529–5541, Dec. 2019.
- [13] M. S. Trotter, J. D. Griffin, and G. D. Durgin, "Power-optimized waveforms for improving the range and reliability of RFID systems," in *Proc. IEEE Int. Conf. RFID*, Apr. 2009, pp. 80–87.
- [14] C. R. Valenta and G. D. Durgin, "Harvesting wireless power: Survey of energy-harvester conversion efficiency in far-field, wireless power transfer systems," *IEEE Microw. Mag.*, vol. 15, no. 4, pp. 108–120, Jun. 2014.
- [15] F. Bolos, J. Blanco, A. Collado, and A. Georgiadis, "RF energy harvesting from multi-tone and digitally modulated signals," *IEEE Trans. Microw. Theory Techn.*, vol. 64, no. 6, pp. 1918–1927, Jun. 2016.
- [16] S. Claessens, Y. T. Chang, D. Schreurs, and S. Pollin, "Receiving ASK-OFDM in low power SWIPT nodes without local oscillators," in *Proc. IEEE Wireless Power Transf. Conf. (WPTC)*, Jun. 2019, pp. 20–25.
- [17] C. Im, J.-W. Lee, and C. Lee, "A multi-tone amplitude modulation scheme for wireless information and power transfer," *IEEE Trans. Veh. Technol.*, vol. 69, no. 1, pp. 1147–1151, Jan. 2020.
- [18] S. Claessens, N. Pan, M. Rajabi, D. Schreurs, and S. Pollin, "Enhanced biased ASK modulation performance for SWIPT with AWGN channel and dual-purpose hardware," *IEEE Trans. Microw. Theory Techn.*, vol. 66, no. 7, pp. 3478–3486, Jul. 2018.
- [19] N. Pan, M. Rajabi, S. Claessens, D. Schreurs, and S. Pollin, "Transmission strategy for simultaneous wireless information and power transfer with a non-linear rectifier model," *Electronics*, vol. 9, no. 7, p. 1082, Jul. 2020.
- [20] D. I. Kim, J. H. Moon, and J. J. Park, "New SWIPT using PAPR: How it works," *IEEE Wireless Commun. Lett.*, vol. 5, no. 6, pp. 672–675, Dec. 2016.
- [21] H. Abbasizadeh, S. Y. Kim, B. S. Rikan, A. Hejazi, D. Khan, Y. G. Pu, K. C. Hwang, Y. Yang, D. I. Kim, and K.-Y. Lee, "Design of a 900 MHz dual-mode SWIPT for low-power IoT devices," *Sensors*, vol. 19, no. 21, p. 4676, Oct. 2019. [Online]. Available: <https://www.mdpi.com/1424-8220/19/21/4676>
- [22] S. Claessens, N. Pan, D. Schreurs, and S. Pollin, "Multitone FSK modulation for SWIPT," *IEEE Trans. Microw. Theory Techn.*, vol. 67, no. 5, pp. 1665–1674, May 2019.
- [23] A. Harish and M. Sachidananda, *Antennas and Wave Propagation* (Oxford Higher Education). Oxford, U.K.: Oxford Univ. Press, 2007. [Online]. Available: <https://books.google.co.jp/books?id=yjY3ngEACAAJ>
- [24] D. Pozar, *Microwave Engineering*, 4th ed. Hoboken, NJ, USA: Wiley, 2011. [Online]. Available: <https://books.google.co.jp/books?id=JegbAAAQBAJ>
- [25] N. Pan, D. Belo, M. Rajabi, D. Schreurs, N. B. Carvalho, and S. Pollin, "Bandwidth analysis of RF-DC converters under multisine excitation," *IEEE Trans. Microw. Theory Techn.*, vol. 66, no. 2, pp. 791–802, Feb. 2018.
- [26] N. Shariati, J. R. Scott, D. Schreurs, and K. Ghorbani, "Multitone excitation analysis in RF energy harvesters—Considerations and limitations," *IEEE Internet Things J.*, vol. 5, no. 4, pp. 2804–2816, Aug. 2018.
- [27] Y. Huang and B. Clerckx, "Large-scale multiantenna multisine wireless power transfer," *IEEE Trans. Signal Process.*, vol. 65, no. 21, pp. 5812–5827, Nov. 2017.
- [28] V. Liu, A. Parks, V. Talla, S. Gollakota, D. Wetherall, and J. R. Smith, "Ambient backscatter: Wireless communication out of thin air," *ACM SIGCOMM Comput. Commun. Rev.*, vol. 43, no. 4, pp. 39–50, Sep. 2013, doi: [10.1145/2534169.2486015](https://doi.org/10.1145/2534169.2486015).
- [29] Coilcraft. (2020). *Chip Inductors 0603CS (1608)*. Accessed: Oct. 15, 2020. [Online]. Available: <https://www.coilcraft.com/getmedia/022eb894-7253-40d0-b07c-650d362fc80e/0603cs.pdf>
- [30] V. Talla, B. Kelloog, S. Gollakota, and J. R. Smith, "Battery-free cellphone," *Proc. ACM Interact. Mob. Wearable Ubiquitous Technol.*, vol. 1, no. 2, pp. 25:1–25:20, Jun. 2017, doi: [10.1145/3090090](https://doi.org/10.1145/3090090).
- [31] *Wireless Technology Services*. Accessed: Feb. 10, 2016. [Online]. Available: <http://www.powercastco.com/>
- [32] A. S. Boaventura and N. B. Carvalho, "Maximizing DC power in energy harvesting circuits using multisine excitation," in *IEEE MTT-S Int. Microw. Symp. Dig.*, Jun. 2011, pp. 1–4.



**TAKASHI IKEUCHI** (Member, IEEE) was born in 1991. He received the B.Eng. degree from the Department of Electronics and Electrical Engineering, Keio University, in 2016, and the M.S. degree from the Department of Information Science and Technology, The University of Tokyo, in 2018. He is currently pursuing the Ph.D. degree. His research interests include low complexity computation methods in wireless communication, the application of wireless power transfer systems, and simultaneous wireless information and power transfer.



**YOSHIHIRO KAWAHARA** (Member, IEEE) was born in 1977. He received the B.E., M.E., and Ph.D. degrees in information communication engineering from The University of Tokyo, Tokyo, Japan, in 2000, 2002, and 2005, respectively.

In 2005, he joined the Faculty of The University of Tokyo. He was a Visiting Scholar with the Georgia Institute of Technology, Atlanta, GA, USA, in 2011. He was a Visiting Assistant Professor with MIT Media Lab in 2013. He is currently a Professor with the Department of Electrical Engineering and Information Systems, The University of Tokyo. He is also a Director of the Research Institute for Inclusive Society through Engineering, The University of Tokyo. His research interests include the Internet of Things and digital fabrication. He is also a member of the Institute of Electronics, Information and Communication Engineers (IEICE), Japan, and the Information Processing Society of Japan (IPSI). He is also a committee member of IEEE MTT TC-24 (RFID Technologies). He was a recipient of the JSPS Award of the 2011, and the 2013 Best Paper Award of the ACM UbiComp. He is also an Associate Editor of *Proceedings of the ACM on Interactive, Mobile, Wearable and Ubiquitous Technologies (IMWUT)* and IEEE PERSASIVE COMPUTING.

...